

# Chemical State Analysis by X-ray Emission Spectroscopy

Hikari Takahara\*, Takashi Shoji\*\* and Yoshiaki Ito\*\*

## Abstract

X-ray emission spectroscopy (XES) is a chemical state analysis method. It is possible to show the change in a compound's bonding state profile by measuring fluorescent X-rays with high energy resolution. Recently, the XES method has been evaluated in the field of advanced materials such as battery materials and catalysts, and the need for laboratory spectrometers is increasing. We are evaluating the applicability of Si-based negative electrode materials and next-generation battery materials for lithium-ion batteries using double-crystal spectroscopy with high-energy resolution. Quantitative analysis results of Li–Si alloy composition and side reaction products were reported based on changes in the Si  $K\beta$  spectral profile during electrochemical charging and discharging. It is known that the X-ray emission spectrum changes depending on the chemical state of the material, but the technique is not actively applied to chemical state analysis currently. In this paper, as the basis for describing the X-ray emission analysis method, we explain the optical system required to obtain high resolution, describe the interpretation of the X-ray emission spectrum and spectral changes due to the chemical state, and introduce application examples.

## 1. Introduction

Chemical state analysis determines what kinds of chemical species are present in sample components. X-ray Absorption Spectroscopy (XAS), X-ray Photoelectron Spectroscopy (XPS), Electron Energy Loss Spectroscopy (EELS) and Electron Probe Micro Analyzer (EPMA) for micro area analysis using electron beams, and Soft X-ray Emission spectroscopy (SXES) are widely used for chemical state analysis. X-ray emission spectroscopy (XES) is another chemical state analysis method, and the profile change in the emission spectrum measured with high energy resolution can be related to the chemical bonding state. While the typical energy resolution of wavelength dispersive X-ray fluorescence analysis (WDXRF), which is generally used for elemental analysis, is several tens of eV in the half width of Cu  $K\alpha$ , for chemical state analysis, energy resolution of about 1/10 of that (several eV in the half width of Cu  $K\alpha$ ) is required. Therefore, double-crystal spectroscopy has often been used for XES. Table 1 shows analytical characteristics of the methods.

When a sample is irradiated with X-rays, the atoms in the sample absorb the X-rays and are ionized by the X-rays exciting the electrons in the inner shells. Then electron transition from the outer shell to the holes in the inner shell occurs. The electron transition energy corresponds to the X-ray emission energy in the XES process. Figure 1 shows a comparison between the  $SK\alpha$  X-ray emission spectrum of sodium thiosulfate and the WDXRF spectrum of the same compound with single-crystal spectroscopy. With the energy resolution of single-crystal spectroscopy, only one peak is observed (blue line in Fig. 1), but when measured by double-crystal spectroscopy, a fine structure consisting of three

peaks is observed (black line in Fig. 1). Since  $S^{2-}$  and  $S^{6+}$  are present in a 1 : 1 ratio in sodium thiosulfate, this is interpreted as the overlap of the two chemical states (Fig. 1, black dashed line)<sup>(1), (2)</sup>. The  $K\alpha$  line is attributed to the transition from the 2p state to the 1s state ( $2p \rightarrow 1s$ ), and the 2p state has fine structure,  $2p_{3/2}$  and  $2p_{1/2}$ , due to spin–orbit interaction. Therefore, the  $K\alpha$  spectrum consists of two peaks,  $2p_{3/2} \rightarrow 1s$  ( $K\alpha_1$ ) and  $2p_{1/2} \rightarrow 1s$  ( $K\alpha_2$ ), and the intensity ratio is 2 : 1 based on the transition probability. Thus, the X-ray emission spectrum reflects the chemical state and spin state of the atom, so the profile change can be used for chemical state analysis.

The first observation that the X-ray emission spectrum changes under the influence of chemical bonding was performed by Lindh and Lundquist<sup>(3)</sup>. They pointed out that the Cl  $K\beta$  spectrum changed depending on the chemical bonding state of the materials. In the 1930s and 1960s, Compton<sup>(4)</sup>, Parratt<sup>(5), (6)</sup>, Bearden<sup>(7)</sup>, and Deslattes<sup>(8)</sup> developed various types of double-crystal spectrometers and evaluated their emission spectra. In the 1970s, Goshi developed a double-crystal spectrometer that could scan a wide area, and then jointly developed a product with Rigaku Denki Kogyo (currently Rigaku)<sup>(9)–(11)</sup>. Using this spectrometer, X-ray emission spectra of elements such as Na, Al, Si, P, S, Ti, Cr, and Mn, all related to steel materials such as slag and glass, were reported<sup>(12)</sup>. While the XPS and XAS methods using synchrotron radiation became widespread in the 1990s, the XES method has rarely been used for practical analysis and is mainly used for basic research of physical properties, such as natural width in the emission spectrum and spectroscopic interpretation<sup>(13)–(16)</sup>. Recently, however, after adopting condensing optical systems with spherical curved crystals<sup>(17)</sup> and 2D detectors<sup>(18)</sup>, and incorporating new technologies such as CCD cameras<sup>(19)</sup> and 2D

\* SBU-WDX, X-ray Instrument Division, Rigaku Corporation.

\*\* XRF, X-Ray Research Laboratory, Rigaku Corporation.

**Table 1.** Characteristics of chemical analysis techniques.

Method	XES	XAS	XPS	EPMA	EELS
	X-ray Emission Spectroscopy	X-ray Absorption Spectroscopy	X-ray Photoelectron Spectroscopy	Electron Probe Micro Analysis	Electron Energy Loss Spectroscopy
Probe	X-ray	X-ray	X-ray	Electron	Electron
Signal	XRF	X-ray	Electron	X-ray	Electron
Analysis depth	μm	μm	nm	nm	nm
Analysis area	mm	mm	μm	μm	nm
Atmosphere	Air/gas/vacuum	Air/gas/vacuum	Ultrahigh vacuum	High vacuum	Ultrahigh vacuum
Characteristics	Spectral analysis of X-ray emission (fluorescent X-rays) by X-ray irradiation. Generally, hard X-rays are used. The profile changes depending on the spin state and the coordination environment.	X-ray absorption analysis by energy scanning of irradiated X-rays. Chemical state analysis by chemical shift of XANES and local structure analysis by EXAFS are common. Synchrotron radiation is mainly used.	Chemical state analysis based on the binding energy of electrons. The chemical shift is large and the versatility is high. Surface sensitive.	Spectral analysis of soft X-ray emission (SXES) associated with ionization by electron beam irradiation. The chemical shift is large due to the outer shell transition. It can also be used in combination with SEM.	Analysis of electron energy loss in electron beam irradiation. The chemical state is analyzed from the change in the interaction between the electron and the sample. It can also be used in combination with TEM.

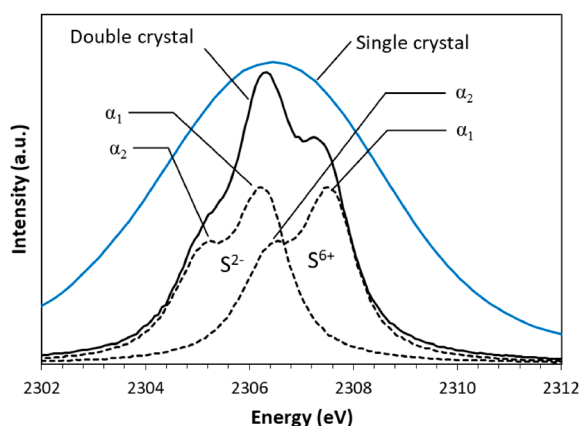


**Fig. 1.** S  $K\alpha$  spectra of sodium thiosulfate  $\text{Na}_2\text{S}_2\text{O}_3$  obtained by double-crystal spectroscopy and single-crystal spectroscopy. Double-crystal spectroscopy (black line) Measurement conditions: Double-crystal spectrometer (Rigaku), X-ray source: Rh Target X-ray tube, 30 kV–100 mA, Analytical crystals: Ge (111)+Ge (111), Detector: F-PC, step scan: 0.005°/step, 1s/step. Single crystal spectroscopy (blue line) Measurement conditions: ZSX Primus IV, X-ray source: Rh target X-ray tube, 30 kV–100 mA, Analytical crystal: Ge (111), detector: F-PC, continuous scan: 3°/min.

superconducting detectors<sup>(20)</sup>, there has been active development of laboratory XES spectrometers<sup>(21), (22)</sup>. These spectrometers have been applied to advanced research in materials such as catalysts and battery materials<sup>(23)–(28)</sup>.

Currently, we are conducting research into the application of the XES method to battery materials using double-crystal spectroscopy<sup>(29), (30)</sup>. Silicon is a potential element as a high-capacity negative

electrode in lithium-ion batteries for electric vehicles, and active research and development is being carried out. Crystalline Si transforms to Li–Si alloy during charging and then to amorphous Si after discharging in the electrochemical reaction of the Si anode. In addition to the reaction of metallic Si,  $\text{SiO}_2$  and lithium silicate are also related to the charge/discharge reaction in the  $\text{SiO}$  negative electrode. We clarified the profile changes of the Si  $K\beta$  spectrum during the charge/discharge reaction of Si-based electrode materials, and then quantified the amount of Li in the Si structure and the side reaction products using linear combination fitting. In this paper, we explain the optical system of the spectrometers, discuss the interpretation of the X-ray emission spectra using Si and Mn as examples, and explore spectral changes due to the chemical compound effect. Furthermore, an example of the application of XES to quantitative analysis of hexavalent Cr is shown and compared with the X-ray Absorption Near Edge Structure (XANES) spectrum of the XAS method, which is more frequently used in chemical state analysis.

## 2. Optical Systems for X-ray Emission Analysis

Analyzing crystals are widely used for X-ray spectroscopy, and the principle is based on Bragg's law,

$$n\lambda = 2d \sin \theta.$$

X-rays of wavelength  $\lambda$  are reflected under the above condition where  $d$  is the distance between the lattice planes,  $\theta$  expresses the X-ray glancing angle on the crystal surface and  $n$  is an integer. An X-ray spectroscope is designed with an appropriate analyzing crystal and the geometry of the incident angle and the detector are determined by the target X-ray wavelength range. When the glancing angle between the incident

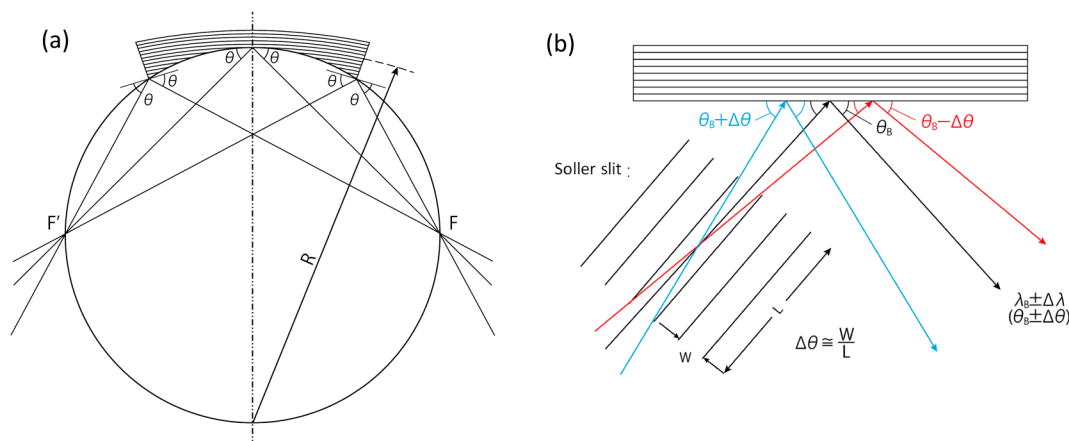


Fig. 2. Schematic diagrams of Johansson-type centralized optical system (a) and parallel optical system (b).

X-rays and the crystal surface is  $\theta$ , the detector should be positioned at the angle  $2\theta$  relative to the incident X-rays. Therefore, specifications and measurement conditions are often displayed in  $2\theta$ . High-energy resolution spectroscopy requires analyzing crystals with high reflectivity and high crystallinity (crystal perfection), such as Si (220), Ge (220), Ge (111), and InSb (111)<sup>(31)</sup>. Also, the wavelength ranges of the K lines of light elements and the L lines of heavy elements are affected by absorption due to the atmosphere, so a vacuum chamber of about 5 Pa is required.

Figure 2 shows a schematic diagram of a Johansson-type focusing spectrometer using a curved crystal and a parallel beam spectrometer using flat crystals as typical systems. In the Johansson-type spectrometer, a curved crystal having Bragg planes with a radius of curvature  $R$  has a curved optical surface with a diameter  $R$  and is placed on the circle with the same diameter (Roland circle), and X-rays emitted from a position  $F$  on the Roland circle are reflected and focused at a position  $F'$ , which is on the opposite side of the circle from the emission point  $F$  according to Bragg's law. By moving the  $F$  position and the corresponding  $F'$  position, the diffraction angle  $\theta$  is varied, the wavelength of the diffracted X-rays is changed, and the X-ray spectrum is acquired. With this optic, when the position of the emission point deviates from the Roland circle, the incidence angle of the X-ray on the crystal differs, so the wavelength of the diffracted X-rays is sensitive to changes in the source size and position of the emitted X-rays. Therefore, a smaller emission source or a finer slit on the Roland circle and a longer distance  $R$  are required to improve the energy resolution. A spectrometer such as the Johansson-type is used in EPMA using an electron beam probe because the X-ray emission area irradiated by the electron beam is easily acquired with a size as small as  $\mu\text{m}$ . When X-rays are used as an irradiating probe, because of the difficulty for X-rays to be focused on a sample at a small enough size, it is necessary to provide a very narrow one-dimensional slit on the Roland circle between the sample and the crystal; however, a decrease in intensity

is inevitable. Therefore, a parallel beam spectrometer is adopted in WDXRF single crystal spectroscopy. When using a flat crystal, a Soller slit is installed in front of the crystal because it is the angle of dispersion ( $\Delta\theta$ ) of the incident X-rays to the crystal—not the incident position of the incident X-rays—that affects the energy resolution. If the slit spacing of the Soller slit is  $W$  and the length is  $L$ ,  $\Delta\theta$  is proportional to  $W/L$ . Realistically considering the decrease in X-ray intensity and the size of the spectrometer,  $W$  is on the order of several hundred  $\mu\text{m}$  and  $L$  is a few cm (generally less than 10 cm). The energy spread with respect to  $\Delta\theta$  obtained by a simple parallel optics is limited to several tens of eV. Thus, in single crystal spectroscopy<sup>(32)</sup>, the spectrum has a poor fine structure as shown in Fig. 1 (blue line). Spectra obtained by single crystal spectroscopy that do not depend on the chemical state are suitable for quantitative analysis of elements.

Double-crystal spectroscopy is easy to understand intuitively if you assume that another spectral crystal is used as an ideal Soller slit to obtain a parallel beam, but in reality, the first crystal is not just about functioning as a simple Soller slit. Figure 3 shows a schematic diagram of the  $(++)$  and  $(+-)$  configurations in double-crystal spectroscopy. In the  $(++)$  configuration (anti-parallel configuration) of the same two crystals, X-rays of wavelength  $\lambda_B$  at diffraction angle  $\theta_B$ , which is determined by the angle  $\pi - 2\theta_B$  between the two crystals, can be reflected with high resolution (Fig. 3(a)). It is assumed that X-rays of  $\lambda_B \pm \Delta\lambda$  having a certain wavelength range are reflected by the first crystal. Of these,  $\lambda_B + \Delta\lambda$  (red line) are reflected at an angle  $\theta_B + \Delta\theta$  by Bragg diffraction. Since this line is incident on the second crystal at  $\theta_B - \Delta\theta$ , it does not satisfy Bragg's equation and is not reflected. Similarly,  $\lambda_B - \Delta\lambda$  (blue line) is reflected on the first crystal at an angle  $\theta_B - \Delta\theta$ , and is not reflected on the second crystal because it is incident on  $\theta_B + \Delta\theta$ . Based on such a mechanism, the double-crystal spectroscopy can obtain a spectrum with high energy resolution with a fine structure as shown in Fig. 1 (black line). The  $(+-)$  configuration (parallel configuration) of the same two crystals is

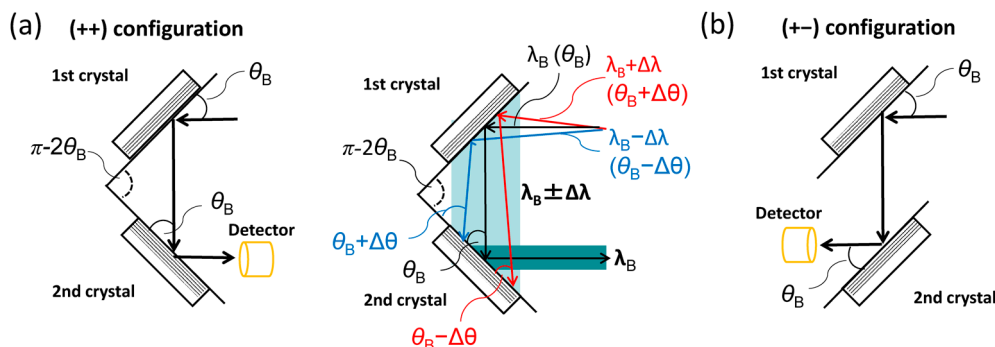


**Fig. 3.** Schematic diagrams of ++ configuration (a) and +- configuration (b) of the double-crystal spectroscopy.

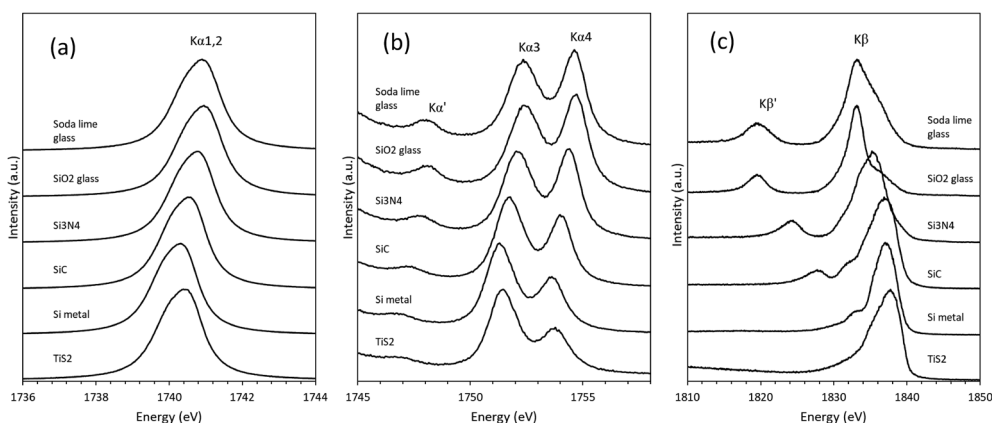


**Fig. 4.** X-ray emission spectra of various Si compounds. Si  $K\alpha_{1,2}$  line (a), Si  $K\alpha_{3,4}$  satellite line (b), Si  $K\beta$  line (c). Measurement conditions: Double-crystal spectrometer (Rigaku), X-ray source: Rh target X-ray tube, 30 kV–100 mA, Analytical crystal: InSb (111)+InSb (111), Detector: F-PC, Step scan: 0.005°/step, 1s/step (a), 0.01°/step, 1–3s/step (b), 0.01°/step, 3–14s/step (c), Analysis area: 30 mm.

non-dispersive; that is, all the X-rays reflected by the first crystal are also reflected by the second crystal. This configuration is used for basic research on reflection by crystals and control of the beam direction with synchrotron radiation (Fig. 3(b)).

Double-crystal spectrometers are roughly classified into two types: narrow-range and wide-range. In the narrow-range type, the angle of the first crystal is fixed at a certain angle and only the second crystal moves about its axis to acquire the scan profile. A divergent beam instead of a parallel beam is incident to the first crystal, and the X-rays with a certain wavelength range equivalent to  $\theta_B \pm \alpha^\circ$  are reflected at the same time. The second crystal scans within its angular range to obtain a spectroscopic spectrum. In this method, the continuous spectrum is limited to the angular range reflected by the first crystal. For example, the continuous angular range of the double-crystal spectrometer developed by Deslattes in the 1960s is  $8^\circ (\pm 4^\circ)^{(8)}$ . This angular range is sufficient to study the spectral structures of Si  $K\alpha_{1,2}$ , Si  $K\alpha_{3,4}$  lines, and Si  $K\beta$  lines, which will be described later, (about  $2^\circ$  in  $2\theta$ ), but it is not enough to obtain all the lines continuously at once, which would require a scan range of about  $20^\circ$  in  $2\theta$ . On the other hand, in the wide-range type, both the first crystal and the second

crystal move synchronously. Therefore, it is necessary to match the incident angle of the X-rays on the first crystal with the incident angle of the X-rays diffracted by the first crystal on the second crystal. The double-crystal spectrometer developed by Goshi in the 1970s is one of the few wide-range type. It enables the automation of angular scanning using a mechanical link system with stationary and planetary gears<sup>(9)</sup>. All emission spectra published in this paper were measured using this wide-range double-crystal spectrometer (manufactured by Rigaku Denki Kogyo (currently Rigaku)).

### 3. Chemical Compound Effect on X-ray Emission Spectrum

Figure 4 shows the emission spectra of Si  $K\alpha_{1,2}$ ,  $K\alpha_{3,4}$  satellite, and  $K\beta$  rays in various Si compounds (Si,  $Ti_2Si$ , SiC,  $Si_3N_4$ ,  $SiO_2$ , soda lime glass) measured by a double-crystal spectrometer. Change in peak energy (chemical shift) due to the chemical compound is observed in the Si  $K\alpha_{1,2}$  spectra, and the chemical shift between Si and  $SiO_2$  is approximately 0.6 eV. This chemical shift is due to the difference in the bond state of Si and is assumed to reflect the effective nuclear charge of Si<sup>(33)</sup>. The profile change of the Si  $K\beta$  spectra is more remarkable than that of the  $K\alpha$  spectra. It can



Fig. 5. Relationship between Si emission spectra and energy level diagram.

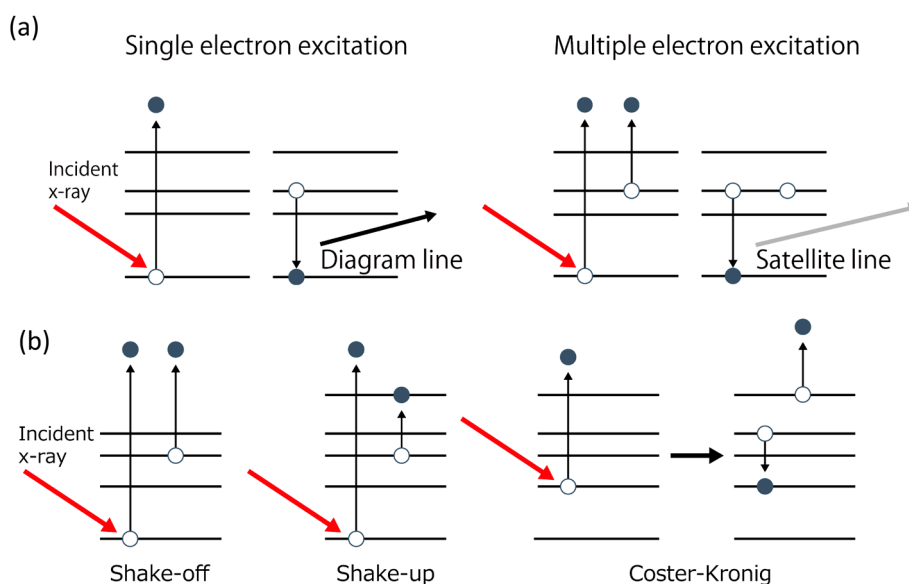
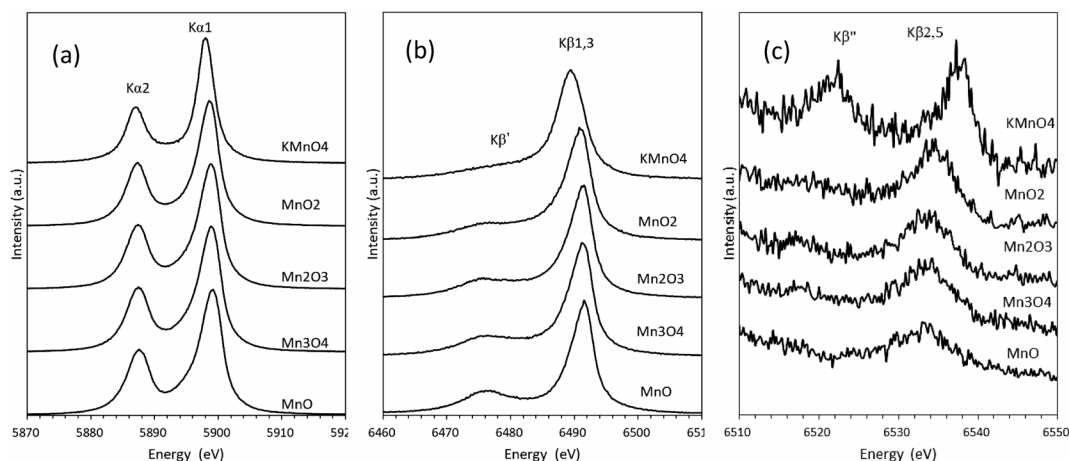


Fig. 6. Conceptual diagram of the generation process of diagram lines and satellite lines (a). Schematic diagram of Shake process and Coster–Kronig transition associated with ionization of K shell (b).

be seen that the chemical shift between Si and SiO<sub>2</sub> is as large as approximately 5 eV, and the width and asymmetry property of the peak profile also change. Figure 5 displays the spectral lines and energy level diagram for Si. The Si K $\alpha_{1,2}$  lines are generated by the transitions from 2p to 1s, and the K $\beta$  lines are by the transitions from 3p to 1s. The K $\beta$  line is the emission spectrum arising from the electrons in the M shell states, which are the valence band. It is believed that the chemical shift increases reflect the difference in the chemical binding state. In covalently bonded oxide and nitride compounds, the K $\beta'$  spectrum appears on the low-energy side, which is explained as the transition of the molecular orbitals of O<sub>2s</sub> and N<sub>2s</sub>. Since this K $\beta'$  spectrum does not appear in Si metal or silicates, there is a report that the degree of oxidation of Si metal can be analyzed from the intensity ratio of K $\beta'$  and K $\beta_{3,4}$ <sup>(34)</sup>. Since the K-line spectrum of SiO<sub>2</sub> is the same for crystalline and amorphous states, it is considered

that the XES method better reflects the coordination environment in the first coordination sphere rather than the long-range structure. Also, the K $\beta$  spectrum of soda lime glass shows a remarkable spread in the profile compared to SiO<sub>2</sub>. The emission spectra of Si in alkaline silicate glasses have been studied in detail, and the spread of the Si K $\beta$  profile is associated with an increase in non-crosslinked oxygen. In addition, correlation between the amount of alkali contained in the glass and the chemical shift of Si K $\beta$  has been reported<sup>(35)</sup>.

While Si K $\alpha_{1,2}$  and Si K $\beta$  are transition lines that occur due to relaxation of a single vacancy state (diagram lines), K $\alpha_{3,4}$  and K $\alpha'$  lines are radiated by relaxation of a double vacancy state. These spectra are called satellites because they are observed with weak relative intensities at energy values far from the diagram line. Figure 6 shows a conceptual drawing of the diagram line and satellite line. Multiple ionization in which the outer shell electron is excited to the



**Fig. 7.** Mn  $K\alpha_{1,2}$  line (a), Mn  $K\beta_{1,3}$  line and  $K\beta'$  satellite line (b), Mn  $K\beta_{2,5}$  line and  $K\beta''$  satellite line (c) of various Mn compounds. Measurement conditions: Double-crystal spectrometer (Rigaku), X-ray source: Rh target X-ray tube, 40kV–60mA, Analytical crystal: Ge (111)+Ge (111), Detector: F-PC, Step scan: 0.001°/step, 1s/step (a), 0.001°/step, 2s/step (b) (c), Analysis area: 30 mm.

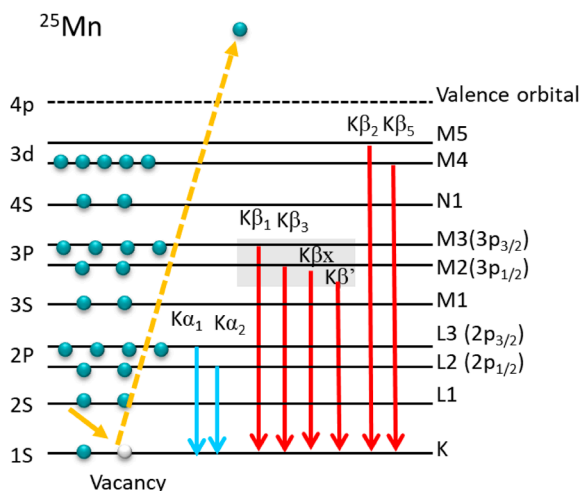


**Fig. 8.** Relationship between Mn emission spectrum and energy level.

extra atomic or valence band at the same time as the emission of the inner shell electron by the incident X-rays is called the Shake process. Shake processes by the ionization of the K shell electron, L shell electron, and M shell electron exist. It tends to occur in light elements with low ionization energies, and in Si, the probability of a satellite due to ionization of K and L shell electrons is 20% or more<sup>(36)</sup>. On the other hand, the Coster–Kronig transition, the name for the multiple ionization of heavy elements, is a phenomenon in which electrons in the outer shell are excited by the surplus energy generated by relaxation in an electron shell with multiple subshells such as L orbitals. It is a kind of Auger transition. The appearance of satellite lines in the L-line spectrum of an element with a large atomic number and the increase in the half width in the  $K\alpha_2$  spectra of the 3d transition metals are explained by the Coster–Kronig transition<sup>(37), (38)</sup>.

Figures 7 and 8 show Mn K emission spectra for various manganese oxides and the energy level diagram,

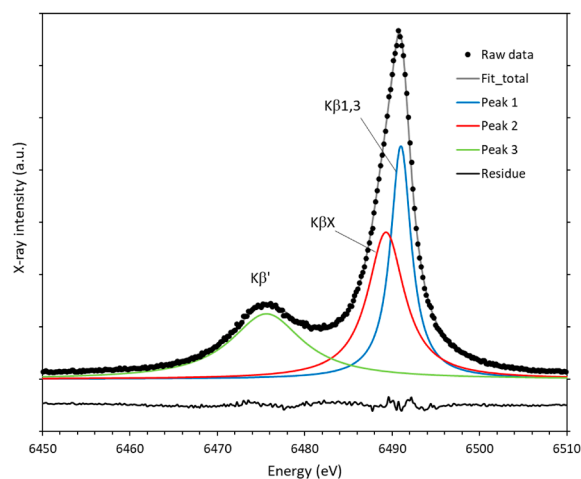


**Fig. 9.** Attribution of Mn  $K\beta$  spectrum in MnO. Peak deconvolution was performed by symmetric Lorentz function.

respectively. Compared with the Si K spectra, the Mn  $K\alpha$  and  $K\beta$  spectra have less change in peak profile due to chemical state. This is because in Mn, 4s electrons and 3d electrons exist in the outer shell and the shielding effect works for the 2p states and the 3p states in which K line emissions are involved, so that the spectrum is not easily affected by the chemical compound effect. However, when observed in detail, the peak energy of the  $K\alpha_{1,2}$  spectrum shifts to the higher energy side as the formal valences of  $K_2MnO_4$ ,  $MnO_2$ , ...  $MnO$  and Mn decrease from 7-valent to divalent (Fig. 7(a)). It can also be seen that the full width at half maximum (FWHM) of the peak profile becomes widened, and it is not symmetric but broader on the low energy side. The FWHM values and asymmetry depend on the degree of exchange interaction between the total spins of 2p electrons and the total spins of 3d electrons. In other words, when an electron transits from the 2p state to the hole state created in the 1s state, the energy level

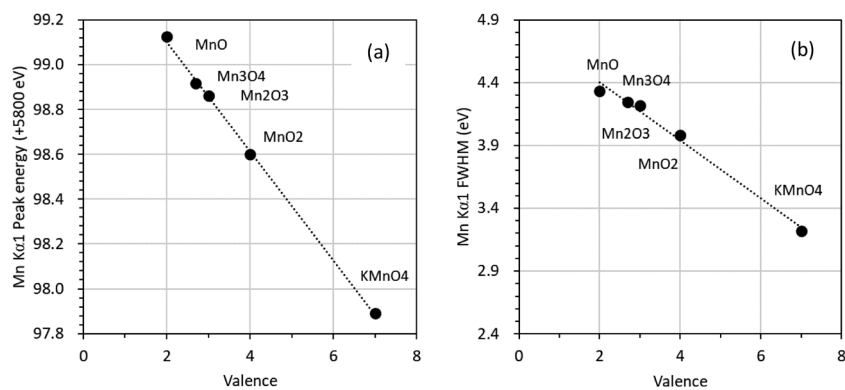


**Fig. 10.** Correlation of profile parameters with valence in Mn oxide, peak energy (a) and full width at half maximum (FWHM) (b) of Mn  $K\alpha_1$  line. The parameters were calculated by symmetric Lorentz function fitting.

in the final state splits due to the 2p–3d spin exchange interaction. Therefore, the larger the contribution of 3d electrons (the smaller the formal value number), the larger the FWHM and asymmetry of the  $K\alpha_{1,2}$  lines. Similarly, the exchange interaction between all spins of 3p electrons and all spins of 3d electrons contributes to the  $K\beta$  line, and it is interpreted as an overlap of the spectrum containing  $K\beta_{1,3}$  lines and the related multiple transitions with different spin states (Fig. 9)<sup>(39)</sup>. The  $K\beta_{2,5}$  lines are transitions involving the 3d and 4p states of the valence band, and the  $K\beta''$  satellite lines are transitions from the 2s state of O, both of which are explained using molecular orbital theory (Fig. 7(c)). Figure 10 shows the correlation between the formal valences of Mn and the peak energies or FWHM values of the Mn  $K\alpha_1$  line in manganese oxides. The formal valence and these parameters show a linear relationship. In addition, the chemical shift and intensity ratio of  $K\beta_{1,3}$  and  $K\beta''$  satellite lines are also related to the formal valence band<sup>(40)</sup>. In this way, the correlation with the emission spectrum parameters is used to estimate and mix the chemical states of unknown compounds.

#### 4. Hexavalent Chromium (Cr(VI)) Identification and Application to Quantitative Analysis

Cr compounds such as  $K_2CrO_4$  and  $CrO_3$  have been used as oxidizing agents and for plating, but hexavalent chromium is extremely toxic and is subject to regulation under the RoHS and WEEE Directives. The analysis method for hexavalent chromium is defined by measuring the absorbance of the eluate, but the time and effort required to prepare the sample and the error due to elution conditions are problematic. Therefore, the use of the XAS<sup>(41)</sup> and XES<sup>(42)</sup> methods has been proposed. Figure 11 shows the X-ray absorption near edge structure (XANES) and the XES spectrum of  $Cr_2O_3$ , which is a compound of  $K_2CrO_4$ ,  $CrO_3$  and Cr(III)<sup>(43)</sup>. It is well known that Cr(VI) compounds have higher absorption edge energy than Cr(III) in the XANES spectrum, and a peak near 5990 eV called pre-edge is observed. Figure 12 shows a schematic diagram of the electron configuration of Cr(III) and Cr(VI).

Cr(III) has three d-electrons, while Cr(VI) has no electron in the 3d states. The white line in the XANES spectrum belongs to the transition from 1s to 4p, and the pre-edge peak belongs to the transition from 1s to 3d. Since in this case the 3d states in Cr(VI) are open, the 1s→3d transition probability becomes high and a large pre-edge peak appears. In addition, since Cr in  $K_2CrO_4$  forms a tetrahedral coordination structure with O, the contribution of the 3d4p hybrid orbital becomes large, which causes a large shift of the white line<sup>(44)</sup>. Furthermore, since  $CrO_3$  has two tetrahedral coordinated sites in the crystal structure, it is considered that the pre-edge and absorption edge change is more complicated.

Unlike XANES, which observes the transition energy to the empty orbital, the transition energy of the inner shell of 2p→1s is observed in the XES spectra of  $K\alpha_1$  and  $K\alpha_2$ . Since the influence of the coordination environment of the compound is shielded by the outer shell electrons, the change is small compared to the XANES spectrum. However, in the Cr  $K\alpha_1$  and  $K\alpha_2$  spectra, changes in the peak profile such as chemical shift to the low energy side, decrease in FWHM value, and increase in  $K\alpha_1/K\alpha_2$  intensity ratio are observed in Cr(VI) (Fig. 11(b)). The  $K\alpha_1$  and  $K\alpha_2$  XES spectra between the two trivalent  $Cr_2O_3$  and hexavalent compounds are distinguishable, but there is no significant difference in the  $K\alpha_1$  and  $K\alpha_2$  XES spectra between the hexavalent compounds  $K_2CrO_4$  and  $CrO_3$ . Therefore, it is difficult to distinguish between these two hexavalent compounds. On the other hand, quantitative analysis of Cr(VI) is possible regardless of the compound. The XES spectrum of the mixture of Cr(VI) and Cr(III) was performed by linear combination fitting using the standard spectrum of each pure substance, and the fitting results showed a correlation with the mixing ratio, suggesting the possibility of quantification<sup>(42)</sup>.

#### 5. Conclusion

As a basis for understanding X-ray emission analysis, we explained the conditions for obtaining high resolution with focusing optics and parallel beam optics, and double-crystal spectrometry. In addition,

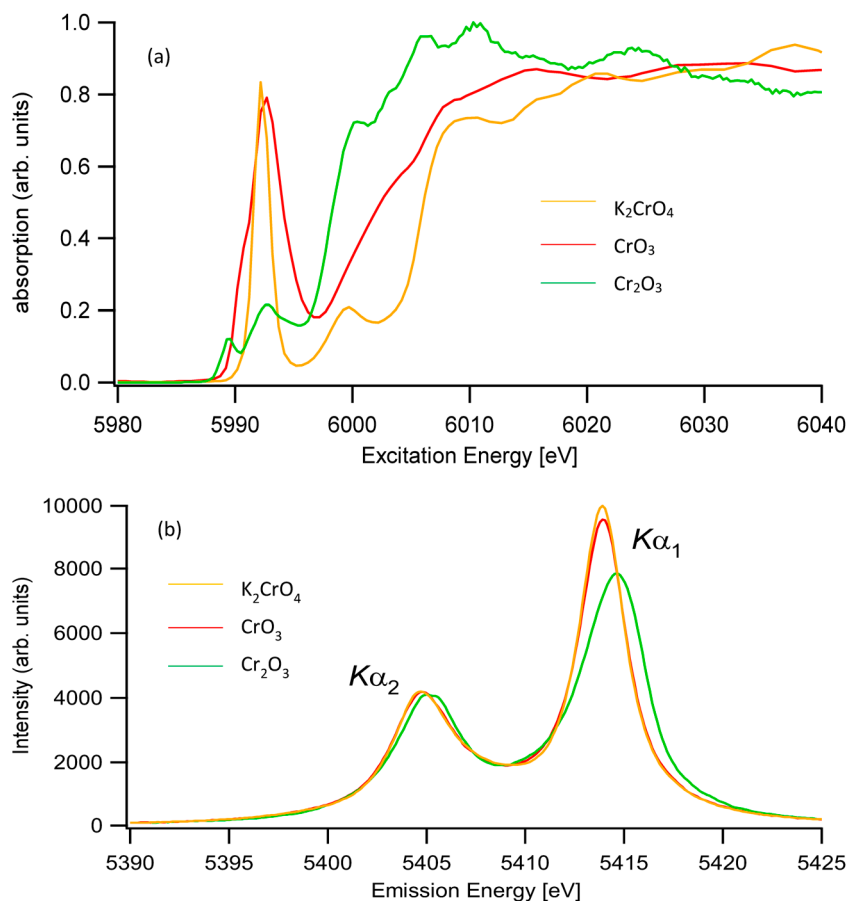


Fig. 11. Cr K absorption edge XANES spectra (a) and Cr  $K\alpha_{1,2}$  line XES spectra (b) in  $K_2CrO_4$ ,  $CrO_3$ , and  $Cr_2O_3$ <sup>(43)</sup>. The spectra were measured at Spring-8 BL1415XU.

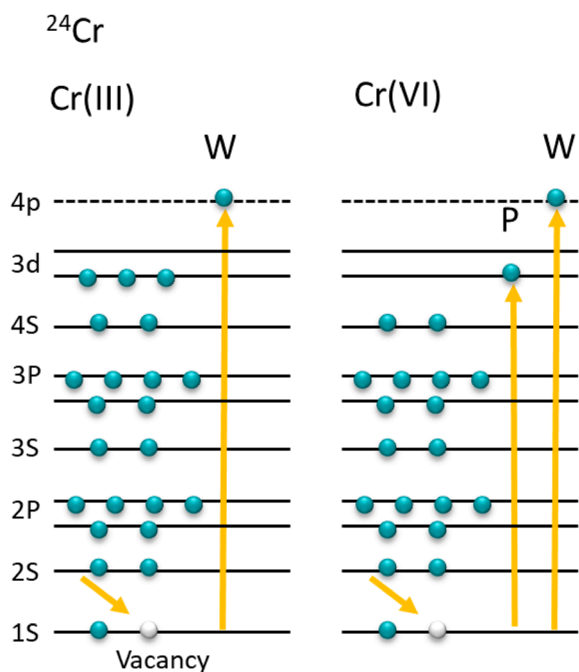


Fig. 12. Relationship between absorption spectra of Cr(III) and Cr(VI) electron configurations. W: White line, P: Pre-edge peak.

the obtained K-line spectra of Si, Mn, and Cr were explained based on the electron configuration and energy levels, and changes in the spectra due to chemical states were described. Since emission spectroscopy deals with inner shell transitions, compound effects do not have much influence on spectral profiles. Therefore, it is necessary to evaluate profile changes using a standard sample and selecting the optimum line to have a larger chemical shift. It is also important to correlate with other analytical methods and to sample models. The methods of chemical state analysis that can be performed in the laboratory are limited, and the XPS method, which is often used at present, requires measurement in a high-vacuum atmosphere. Moreover, since it is a surface analysis technique, bulk information cannot be obtained. The XAS method requires synchrotron radiation and time constraints are unavoidable. Recently, laboratory XES spectrometers incorporating new elemental technologies such as analyzing crystals and detectors and optical systems have been researched and developed. It is expected that the XES method will be used as one of the state analytical methods in the fields of catalysts and batteries in the future.

## References

- (1) Y. Gohshi: Tokyo University, Ph.D. Thesis (1977).
- (2) J. Kawai: Chapter 2 Introduction to X-ray spectroscopy, X-ray, Synchrotron radiation spectroscopy 7, Kodansha Scientific, (2009), 17–22.
- (3) O. Lundquist: *Z. Phys.*, **33** (1925), 901–915.
- (4) A. H. Compton: *Rev. Sci. Instrum.*, **2** (1931), 365–376.
- (5) L. G. Parratt: *Phys. Rev.*, **41** (1932), 553–560.
- (6) L. G. Parratt: *Phys. Rev.*, **49** (1936), 14–16.
- (7) H. H. Roseberry and J. A. Bearden: *Phys. Rev.*, **50** (1936), 204–208.
- (8) R. D. Deslattes: *Rev. Sci. Instrum.*, **38** (1967), 616–620.
- (9) Y. Gohshi, K. Hori, Y. Fukao: *Adv. X-ray. Chem. Anal., Japan*, **14** (1971), 57–72.
- (10) Y. Gohshi, K. Hori, and Y. Fukao: *Spectrochim. Acta B*, **27** (1972), 135–142.
- (11) Y. Gohshi, H. Kamada, K. Kohra, T. Utaka, and T. Arai: *Appl. Spectrosc.*, **36** (1982), 171–174.
- (12) Y. Gohshi: *Bunseki*, **9** (1982), 646–654.
- (13) P. Glatzel and U. Bergmann: *Coord. Chem. Rev.*, **249** (2005), 65–95.
- (14) M. Deutsch, G. Hölzer, J. Härtwig, J. Wolf, M. Fritsch, and E. Förster: *Phys. Rev.*, **A51** (1995), 283–296.
- (15) G. Hölzer, M. Fritsch, M. Deutsch, J. Härtwig, and E. Förster: *Phys. Rev.*, **A56** (1997), 4554–4555.
- (16) Y. Ito, T. Tochio, H. Oohashi, and A. M. Vlaicu: *Rad. Phys. Chem.*, **75** (2006), 1534–1537.
- (17) G. T. Seider, D. r. Mortensen, A. J. Remesnik, J. I. Pacold, N. A. Ball, N. Barry, M. Styczinski, and O. R. Holidn: *Rev. Sci. Instrum.*, **85** (2014), 113906.
- (18) K. Sato, A. Nishimura, M. Kaino, and S. Adachi: *X-ray Spectrometry*, **46** (2017), 330–335.
- (19) L. Anklam, C. Schlesiger, W. Malzer, D. Gröttsch, M. Neitzel, and B. Kanngießer: *Rev. Sci. Instrum.*, **85** (2014), 053110.
- (20) J. W. Fowler, G. C. O. Neil, B. K. Alpert, D. A. Bennett, E. V. Denison, W. B. Doriese, G. C. Hilton, L. T. Hudson, Y.-I. Joe, K. M. Morgan, D. R. Schmidt, D. S. Sweetz, C. I. Szabo, and J. N. Ullmos: *Metrologia*, **58** (2021), 015016.
- (21) W. Malzer, C. Schlesiger, and B. Kanngießer: *Spectrochim. Acta B*, **177** (2021), 106101.
- (22) H. Hayashi and M. Takaishi: *Anal. Sci.*, **36** (2020), 1197–1202.
- (23) C. R. Horne, U. Bergmann, M. M. Grush, R. C. C. Perera, D. L. Ederer, T. A. Callcott, E. J. Cairns, and S. C. Cramer: *J. Phys. Chem. B*, **104** (2000), 9587–9596.
- (24) E. P. Jahrman, W. M. Holden, A. S. Ditter, D. R. Motensen, G. T. Seidler, T. T. Fister, S. A. Kozimor, L. F. J. Piper, J. Rana, N. C. Hyatt, and M. C. Stennett: *Rev. Sci. Instrum.*, **90** (2000), 024106 (2019).
- (25) W. Malzer, D. Gröttsch, R. Gnewkow, C. Schlesiger, F. Kowalewski, B. V. Kuiken, S. DeBeer, and B. Kanngießer: *Rev. Sci. Instrum.*, **89** (2018), 113111.
- (26) K. Sato, T. Yoneda, T. Izumi, T. Omori, S. Tokuda, S. Adachi, M. Kobayashi, T. Murai, H. Tanaka, and M. Yanagida: *Anal. Chem.*, **92**(2020), 758–765.
- (27) M. Kavčič, M. Petric, A. Rajh, K. Isaković, A. Vizintin, S. D. Talian, and R. Dominko: *ACS Appl. Energy Mater.*, **4** (2021), 2357–2364.
- (28) M. Kavčič, K. Bučar, M. Petric, M. Žitnik, I. Arčon, R. Dominko, and A. Vizintin: *J. Phys. Chem. C*, **120**, 24568–24576 (2016).
- (29) H. Takahara, T. Shoji, Y. Ito, N. Kawahara, M. Doui, H. Kobayashi: The 61th Battery Symposium in Japan, 3A10 (2020).
- (30) H. Takahara, T. Shoji, Y. Ito, N. Kawahara, M. Doui, H. Kobayashi: 88th Meeting of the Electrochemical Society in Japan, 1110 (2021).
- (31) N. Kawahara: Chapter 2, Kodansha Scientific, Element technology of X-ray, 2.2.4 Analytical crystals and Artificial multilayer film, X-ray Analysis Method, K. Tsuji and Y. Muramatsu, eds., Kodansha Scientific (2018), 37–40.
- (32) S. Imai, K. Uemura, K. Kodama, Y. Yamamoto: *Adv. X-ray. Chem. Anal., Japan*, **49** (2018), 125–142.
- (33) Z. Liu, S. Sugata, K. Yuge, M. Nagasono, K. Tanaka, and J. Kawai: *Phys. Rev. B*, **69**, 035106, (2004).
- (34) T. Konishi, K. Neki, S. Fukushima, and Y. Gohshi: *Adv. X-ray. Chem. Anal., Japan*, **19** (1988), 87–96.
- (35) T. Maekawa: *Bull. Japan Inst. Met.*, **24**(3), (1985), 186–192.
- (36) T. Mukoyama and K. Taniguchi: *Phys. Rev. A*, **36**, 693 (1987).
- (37) H. Ohashi, Y. Ito, T. Tochio, and T. Mukoyama: *Phys. Rev. A*, **73** (2006), 022507.
- (38) Y. Ito, T. Tochio, M. Yamashita, S. Fukushima, A. M. Vlaicu, L. Syrocki, K. Ślabkowska, E. weder, M. Polasik, K. Sawicka, P. Indelicato, J. P. Marques, J. M. Sampaio, M. Guerra, J. P. Santos, and F. Parente: *Phys. Rev. A*, **97** (2018), 052505.
- (39) G. Peng, F. M. F. deGroot, K. Hamalainen, J. A. Moore, X. Wang, M. M. Grush, J. B. Hastings, D. P. Siddons, W. H. Armstrong, O. C. Mullins, and S. P. Cramer: *J. Am. Chem. Soc.*, **116** (1994), 2914–2920.
- (40) S. Limandri, S. Ceppi, G. Tirao, G. Stutz, C. G. Sánchez, and J. A. Riveros: *Chem. Phys.*, **367** (2001), 93–98.
- (41) K. Nomura and N. Awaji: *Jpn. J. Appl. Phys.*, **45** (2006), L304–306.
- (42) T. Tochio, S. Sakakura, H. Oohashi, H. Mizota, Y. Zou, Y. Ito, S. Fukushima, S. Tanuma, T. Shoji, H. Fujimura, and M. Yamashita: *Anal. Sci.*, **26** (2010), 277–279.
- (43) Y. Ito, S. Fukushima, T. Tochio, K. Yoshii, Y. Yoneda, T. Terasawa: 72th Japanese Conference of Analytical Chemistry, C2001 (2012).
- (44) T. Yamamoto: *Adv. X-ray. Chem. Anal., Japan*, **38** (2007), 45–65.